Magnetic Alignment for Plasmonic Control of Gold Nanorods Coated with Iron Oxide Nanoparticles

Mehedi H. Rizvi, Ruosong Wang, Jonas Schubert, William D. Crumpler, Christian Rossner, Amy L. Oldenburg, Andreas Fery, and Joseph B. Tracy*

Plasmonic nanoparticles that can be manipulated with magnetic fields are of interest for advanced optical applications, diagnostics, imaging, and therapy. Alignment of gold nanorods yields strong polarization-dependent extinction, and use of magnetic fields is appealing because they act through space and can be quickly switched. In this work, cationic polyethyleneimine-functionalized superparamagnetic Fe_3O_4 nanoparticles (NPs) are deposited on the surface of anionic gold nanorods coated with bovine serum albumin. The magnetic gold nanorods (MagGNRs) obtained through mixing maintain the distinct optical properties of plasmonic gold nanorods that are minimally perturbed by the magnetic overcoating. Magnetic alignment of the MagGNRs arising from magnetic dipolar interactions on the anisotropic gold nanorod core is comprehensively characterized, including structural characterization and enhancement (suppression) of the longitudinal surface plasmon resonance and suppression (enhancement) of the transverse surface plasmon resonance for light polarized parallel (orthogonal) to the magnetic field. The MagGNRs can also be driven in rotating magnetic fields to rotate at frequencies of at least 17 Hz. For suitably large gold nanorods (148 nm long) and Fe_3O_4 NPs (13.4 nm diameter), significant alignment is possible even in modest (<500 Oe) magnetic fields. An analytical model provides a unified understanding of the magnetic alignment of MagGNRs.

1. Introduction

The anisotropic shape of gold nanorods (GNRs) endows them with unique wavelength-tunable and polarization-dependent optical properties that find potential applications in photothermal therapy, colorimetric sensing, bioimaging, and optoelectronics.[1–8] Building on the refinement of methods for synthesizing GNRs over the last two decades,[9,10] numerous techniques have been developed for aligning and assembling GNRs, yielding novel optical properties.[11] GNRs have longitudinal and transverse surface plasmon resonances (LSPR and TSPR) that are excited when the electric field of light is oriented along the length and diameter, respectively. The LSPR is more intense than the TSPR, and the wavelength of the LSPR depends on the aspect ratio of the nanorod, which allows tuning into the near-infrared spectrum. Alignment of GNRs allows for selective excitation of the LSPR or TSPR and has been achieved through stretching polymer films,[12–14] electrospinning polymer fibers,[15,16] controlled evaporation-mediated deposition,[17,18] deposition on templates,[19–23] wrinkle-assisted assembly,[24] mechanical brushing,[25] and dispersion with liquid crystals.[26–31] Although some of these techniques for alignment can provide a high degree of ordering, the ability to dynamically align GNRs dispersed in liquids using applied magnetic or electric fields is appealing for its speed and reversibility. Aligning GNRs using electric fields,

M. H. Rizvi, W. D. Crumpler, J. B. Tracy
Department of Materials Science and Engineering
North Carolina State University
Raleigh, NC 27695, USA
E-mail: jbtracy@ncsu.edu
R. Wang, J. Schubert, C. Rossner, A. Fery
Leibniz-Institut für Polymerforschung Dresden e.V.
Institute for Physical Chemistry and Polymer Physics
01069 Dresden, Germany

C. Rossner
Dresden Center for Intelligent Materials (DCIM)
Technische Universität Dresden
01069 Dresden, Germany
A. L. Oldenburg
Department of Physics and Astronomy
University of North Carolina
Chapel Hill, NC 27599, USA
A. Fery
Chair for Physical Chemistry of Polymeric Materials
Technische Universität Dresden
01062 Dresden, Germany

**ADVANCED
SCIENCE NEWS**

www.advancedsciencenews.com

**ADVANCED
MATERIALS**

www.advmat.de

however, requires high field strengths and small, sub-mm electrode separation.[32–36] Optical torque has also been used to align single GNRs in solution but generally requires intense, highly focused light, and is thus restricted to small sample volumes.[37] Applying magnetic fields, in contrast, does not require direct contact of a solution with electrodes and can be performed over large sample volumes.[38,39] While colloidal synthesis of GNRs with precisely engineered optical properties has become commonplace, we are not aware of previous reports of the deposition of magnetic materials onto GNRs together with a demonstration of alignment using magnetic fields, likely due to challenges achieving sufficiently large magnetic anisotropy for magnetic alignment.

Magnetic alignment of GNRs has thus far involved synthesis approaches that impair the optical properties of GNRs, as compared with well-established methods for synthesizing nonmagnetic GNRs coated with cetyltrimethylammonium bromide (CTAB). Specifically, magnetically alignable GNRs thus far have high background extinction, broad LSPRs, and low ratios of LSPR to TSPR extinction. To provide an overview of the state of the field, it is important to briefly review these previous reports. Segmented nanorods have been prepared by electrodepositing alternating layers of Au and Ni rods in porous anodic aluminum oxide templates.[40,41] The segmented nanorods aligned and rotated in a rotating magnetic field.[42–45] In approaches pioneered by Yadong Yin and coworkers, the magnetic shape anisotropy of iron oxide nanorods was utilized to align GNRs. Large (≈200 nm) hematite nanorods were overcoated with Au shells[46] or decorated with GNRs on their surface with approximate (due to the curvature of the hematite nanorods) coalignment of their long axes.[47] In another method, elongated voids within silica nanorods with embedded magnetite (Fe_3O_4) nanorods were filled with gold, resulting in embedded GNRs with their long axes coaligned with the magnetite nanorods.[48] While these studies showed that magnetic alignment of GNRs is possible, introduced important concepts, and demonstrated applications of these materials, the shortcomings in their optical properties are significant. In this work, we address these issues and report magnetic GNRs, in which the narrow and intense LSPR of the GNR core and low background extinction are preserved during assembly of Fe_3O_4 nanoparticles (NPs) on their surface. The NPs do not dramatically alter the optical properties of the GNR cores. GNRs with magnetic overcoatings have potential biomedical applications, for example multimodal imaging and photothermal therapy, which are further supported by the biocompatibility of Au and Fe_3O_4.[49,50] Magnetic alignment and manipulation of GNRs and related anisotropic structures have been applied in magnetochromic sensors,[46,51] photothermal actuators,[52] gyromagnetic imaging,[53] and nano-electromechanical systems like nanomotors for controlled drug release.[43]

Magnetic alignment of anisotropic micro- and nanostructures has been demonstrated by depositing spherical magnetic NPs on their surfaces, including Al_2O_3 microplatelets,[54] cellulose microcrystals,[55] high-aspect-ratio $CaSO_4$ nanorods,[54] polymer microrods,[56] SiC whiskers,[57,58] Te nanorods,[59] Ag nanowires,[60] and carbon nanotubes.[61] Hybrid nanorods composed of spherical magnetic and plasmonic NPs formed using templates can also be aligned in magnetic fields.[62] In general,

assembly approaches using well-optimized methods for homogeneous nucleation and growth of NPs are attractive, because seeded-growth involving a change in composition between the seed and material deposited can be challenging and strongly depends on the specific system. The mechanism of alignment of anisotropic nonmagnetic particles using coatings of magnetic NPs is based on coupling of their magnetic dipoles. For a pair of magnetic NPs that are close enough to have interacting magnetic dipoles, magnetostatics favors alignment of the dimer parallel to an applied magnetic field, giving head-to-tail alignment (negative energy) instead of side-by-side alignment (positive energy). When decorating magnetic NPs on the surface of a larger prolate nanostructure (i.e., nanorod in this work), alignment parallel to the field direction is the state with the lowest magnetostatic energy because the numbers of head-to-tail and side-by-side interactions between adjacent pairs of NPs are maximized and minimized, respectively. Conversely, alignment perpendicular to the long axis exhibits the highest magnetostatic energy by maximizing and minimizing the numbers of side-by-side and head-to-tail interactions, respectively. As a result, these dipolar interactions can impart uniaxial magnetic anisotropy to the nanorod, causing it to align with the field, if the energy barrier $U_{barrier}$ between configurations for parallel and perpendicular alignment is high enough to overcome the contributions of thermal energy to the Brownian motion of the nanorod within a solvent. The magnetostatic origins of the torque that can align anisotropic nanostructures coated with magnetic NPs are closely related to torques that align chains of magnetic particles with applied magnetic fields.[63,64]

Despite several reports of overcoating GNRs with spherical iron oxide NPs,[49,50,65] to the best of our knowledge, alignment of these structures in magnetic fields has not been reported. Alignment of GNRs with low aspect ratios, giving LSPRs of ≈800–1000 nm, is expected to be challenging because $U_{barrier}$ decreases with decreasing aspect ratio, yet there is great interest in GNRs with these aspect ratios for many applications, including imaging and therapy.[2,4,66] If the loading of magnetic NPs is too low or their sizes too small, $U_{barrier}$ is reduced, and magnetic aligment is limited. The nanostructures that have been aligned using coatings of spherical magnetic NPs are generally both large, with at least one dimension exceeding 300 nm,[59] and have high aspect ratios, which both contribute to a higher $U_{barrier}$. For all magnetic alignment approaches, an additional consideration is avoiding undesired agglomeration of structures coated with magnetic NPs, which can occur if the magnetic moments interact too strongly, for example if the magnetic moments of the magnetic NPs are too large, or if they are ferromagnetic. Use of superparamagnetic NPs is helpful for providing large magnetic moments, while avoiding strong long-range interactions.[67]

In this work, we demonstrate and characterize the magnetic alignment of GNRs with overcoatings of superparamagnetic NPs. Mixing GNRs functionalized with anionic bovine serum albumin (BSA-GNRs) and Fe_3O_4 NPs functionalized with cationic polyethyleneimine (PEI-Fe_3O_4 NPs) under optimized conditions yields MagGNRs, consisting of BSA-GNR cores with dense shells of PEI-Fe_3O_4 NPs. Magnetic dipolar interactions among neighboring Fe_3O_4 NPs decorating the GNR core give rise to

magnetic anisotropy, which causes the MagGNRs to align parallel to applied magnetic fields, enabling noncontact, magnetic manipulation of the LSPR and TSPR. Two sizes of GNR cores and Fe_3O_4 satellite NPs are investigated, revealing that both large GNR cores and large Fe_3O_4 NPs are necessary for obtaining significant alignment in magnetic fields. Alignment is observed even in low magnetic fields and begins to saturate at a field of 500 Oe, which is readily obtained using permanent magnets. Multiple methods are employed to comprehensively characterize the magnetic alignment of MagGNRs: transmission electron microscopy (TEM) to directly observe alignment in 2D after drying on substrates, small-angle X-ray scattering (SAXS) to directly measure the distribution of MagGNR orientations in colloidal dispersion, confirm a model for 3D angular distributions, and predict $U_{barrier}$, and polarized optical extinction spectroscopy to characterize the magnetically modulated optical properties and independently validate $U_{barrier}$ under the same model.

2. Results and Discussion

Two different sizes of MagGNRs were synthesized and characterized with a host of methods to probe their structure, chemistry, and optical and magnetic properties, including their organization and response to applied magnetic fields. The discussion focuses chiefly on the large MagGNRs, because they exhibit better alignment in magnetic fields than the small MagGNRs do. For this reason, some of the characterization was performed only on the large MagGNRs. In addition to reporting the alignment of MagGNRs and their novel magneto-optical properties, a major theme in this work is quantifying their alignment and extracting $U_{barrier}$ from this analysis. An analytical model is proposed for the angular orientation distribution of MagGNRs given $U_{barrier}$, which is numerically integrated to predict 2D and 3D order parameters. The model makes possible estimation of $U_{barrier}$ from characterization by TEM, SAXS, and optical extinction spectroscopy.

2.1. Synthesis and Assembly of MagGNRs

Small and large GNRs stabilized by CTAB were synthesized with average dimensions of 78 nm × 21 nm and 148 nm × 47 nm, respectively.[68–70] CTAB was displaced by bovine serum albumin (BSA) protein (Figure S1, Supporting Information), which made the BSA-coated GNRs negatively charged.[71] Spherical oleic acid-stabilized Fe_3O_4 NPs with an average diameter of 13.4 nm were prepared,[72] and the oleic acid was successively replaced with oleylamine[73] and then polyethylenimine (PEI), yielding positively charged PEI-Fe_3O_4 NPs that dispersed in water (Figure S2, Supporting Information). At the pH of 10.6 at which assembly occurs, typical zeta potentials of small and large BSA-GNRs and PEI-Fe_3O_4 NPs are −29, −27, and +3 mV, respectively.

Mixing of BSA-GNRs and PEI-Fe_3O_4 NPs at room temperature initiated electrostatic self-assembly of coatings of the PEI-Fe_3O_4 NPs on the BSA-GNR cores, yielding MagGNRs. Excess PEI-

Fe_3O_4 NPs are then removed via centrifugation. The MagGNRs disperse well in water, which is confirmed by the lack of broadening of the LSPR and the good dispersion shown in TEM images. Good dispersion of MagGNRs is important for alignment in applied magnetic fields, since agglomerates could have multiple and disordered anisotropy axes and different alignment behaviors than individual MagGNRs. MagGNRs have good stability for at least several months when stored in the refrigerator.

2.2. Model for Quantifying Magnetic Alignment and Estimating $U_{barrier}$

Before discussing experimental TEM, extinction spectroscopy, and SAXS measurements, we introduce a unified model for quantifying alignment of MagGNRs from these measurements. We first consider the dipole–dipole interaction between two identical NPs on the surface of a MagGNR, each with magnetic dipole moment **m** induced from an externally applied magnetic field **H**. As we show later, the NPs are superparamagnetic, for which **m** and **H** are co-aligned. If we define γ_{ij} as the angle between **m** and the displacement vector $\mathbf{r}_{ij}$ between the NPs, the magnetic potential energy can be written as (see the Supporting Information)

$$U_{ij}\left(\gamma_{ij}\right) = \frac{\mu_0 |\mathbf{m}|^2}{4\pi |\mathbf{r}_{ij}|^3}\left(1 - 3\cos^2\gamma_{ij}\right) \tag{1}$$

where μ_0 is the permeability of free space. To model the total potential energy of an assembled MagGNR, U_{MagGNR}, we consider it as the sum of the potential energies U_{ij} arising from each pair of NPs decorating the GNR core. In this study, we are primarily interested in the θ dependence of U_{MagGNR}, where θ is defined as the angle between **H** and the long axis of the GNR (**Figure 1**). After performing this summation, the θ dependence may be written as

$$U_{MagGNR}\left(\theta\right) = -nk_BT\cos^2\theta \tag{2}$$
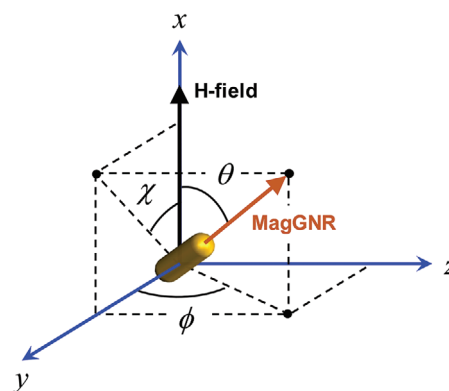
Figure 1. Angles used to describe the orientation of a MagGNR within a magnetic field directed along the x-axis. θ is the angle from the x-axis (**H**-field direction), ϕ is the projected angle in the yz-plane (perpendicular to **H**), and χ is the projected angle in the xy-plane (plane parallel to **H**).

ADVANCED
SCIENCE NEWS

www.advancedsciencenews.com

ADVANCED
MATERIALS

www.advmat.de

where n is a dimensionless number that depends upon $\mathbf{m}$ and the number and positions of the NPs decorating the GNR core. We further note that U_{MagGNR} has a common functional form observed in related systems. The energy of a single-domain magnetic NP by the Stoner–Wohlfarth model with its magnetization in the same direction as $\mathbf{H}$[74] and the potential energy in optical trapping experiments of GNRs both have a $-\cos^2\theta$ dependence.[37] Importantly, n quantifies the magnetic trap depth as a multiple of the thermal energy, k_BT. This can be seen by writing the trap depth as the difference in potential energy between a MagGNR oriented perpendicular (high energy) versus parallel (low energy) to the magnetic field direction

$$U_{barrier} = U_{MagGNR}(90°) - U_{MagGNR}(0°) = nk_BT \tag{3}$$

which corresponds to $n \times 25.9$ meV at room temperature. We expect that n should be $\gtrsim 1$ for significant magnetic alignment.

To characterize the magnetic alignment for a given trap depth, we model the angular distribution function f_θ of an ensemble of MagGNRs in thermal equilibrium according to the canonical ensemble[75]

$$f_\theta = \frac{e^{-U_{MagGNR}(\theta)/k_BT}}{\int_0^{2\pi}\int_0^{\pi} e^{-U_{MagGNR}(\theta')/k_BT}\sin\theta'\,d\theta'\,d\phi'} \tag{4}$$

where ϕ is the projected angle of the GNR into the plane perpendicular to the magnetic trap according to Figure 1. Because U_{MagGNR} is independent of ϕ, the distribution simplifies to

$$f_\theta(n) = \frac{e^{n\cos^2\theta}}{2\pi\int_{-\pi/2}^{\pi/2} e^{n\cos^2\theta'}|\sin\theta'|\,d\theta'} = \frac{e^{n\cos^2\theta}}{Z(n)} \tag{5}$$

where the denominator (partition function Z) depends only on the trap depth n. The limits of integration have been modified such that f_θ is centered at $\theta = 0$, which is more physically relevant for considering deviations in the orientation of MagGNRs from $\mathbf{H}$. Interestingly, Equation (5) is the well-known Maier–Saupe distribution,[76,77] which has been used extensively for modelling nematic ordering, including the alignment of magnetic nanorods.[78] The distribution is normalized such that

$$2\pi\int_{-\pi/2}^{\pi/2} f_{\theta'}|\sin\theta'|\,d\theta' = 1 \tag{6}$$

and the angular probability density is thus $2\pi f_\theta \sin\theta$. This provides a means for predicting metrics, such as the root-mean-squared angle θ_{RMS} (and others in the Supporting Information), which can be obtained by numerically integrating over the distribution as follows

$$\theta_{RMS} = \sqrt{\langle\theta^2\rangle} = \sqrt{2\pi\int_{-\pi/2}^{\pi/2} \theta'^2 f_{\theta'}(n)|\sin\theta'|\,d\theta'} \tag{7}$$

We apply this model below to estimate n from measurements of the MagGNR orientation distributions under different conditions and with different experimental techniques. Knowing n, we then predict θ_{RMS}, and the 2D and 3D order parameters,

S_{2D} and S_{3D} [additional derivations by ensemble averaging in Equation (S24), Supporting Information], and make a comprehensive comparison with experimental results.

2.3. Magnetic Alignment and Transmission Electron Microscopy

MagGNRs align parallel to applied magnetic fields. Dispersions of MagGNRs were dried onto TEM grids under uniform, in-plane 10 kOe magnetic fields by placing the grid between two poles of an electromagnet. Compared to the small MagGNRs, the large MagGNRs have more Fe_3O_4 NPs on their surface, resulting in more magnetic interactions and a larger expected value of $U_{barrier}$. This is consistent with our observation that large MagGNRs show a much higher extent of alignment in magnetic fields than do small MagGNRs, as seen qualitatively by comparing **Figure 2**a,b with Figure 2c,d.

To quantify the extent of alignment, we performed an analysis consistent with 3D characterization while dispersed in water, although subject to the limitations of the 2D nature of TEM images and potential artifacts during drying. The 2D order parameter $S_{2D} = 2\langle\cos^2\chi\rangle - 1$ was calculated from the angular distribution of 200 large MagGNRs dried in applied magnetic fields (Figure S3, Supporting Information).[26,33,79] S_{2D} of 0.70 was obtained for large MagGNRs, which is comparable to reported results for assembly with electric fields and capillary forces.[33,80] For small MagGNRs, S_{2D} is 0.21. For relating these 2D measurements to a 3D system, we can treat the observed orientation distribution on the TEM grid as the projection of the 3D orientation. If the plane of the TEM grid would be in the xy-plane in Figure 1, then χ represents the angle between the long axis of the MagGNR and $\mathbf{H}$ that is measured in 2D TEM images. The polar angle θ, which has projected angle χ in
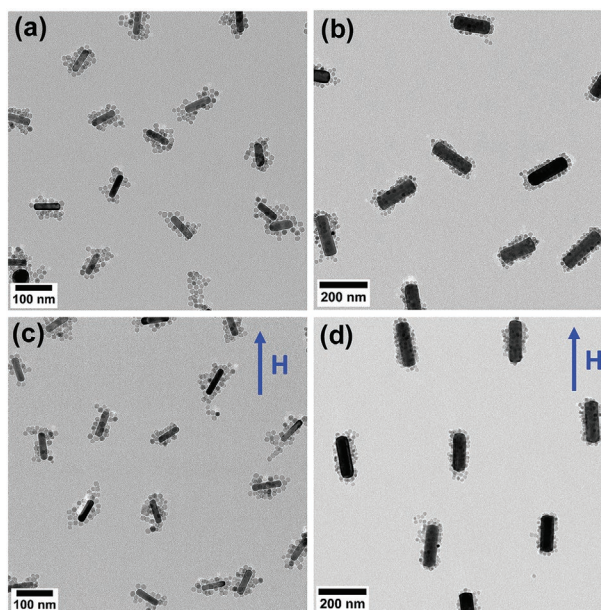
Figure 2. TEM images of MagGNRs dried on TEM grids with or without a 10 kOe magnetic field parallel to the grid and in the vertical direction in the images. a) Small and b) large MagGNRs without field and c) small and d) large MagGNRs dried in the magnetic field.

the plane of the TEM grid, is used to define the 3D orientation distribution f_θ. We find $S_{2D} = 2\langle\cos^2\chi\rangle - 1 = 2\langle\cos\theta\rangle - 1$ (see the Supporting Information). The trap depth parameter n can be extracted by interpolating a curve of predicted S_{2D} with n via numerical integration over the distribution f_θ. Values of n of 1.2 and 4.7 were obtained for small and large MagGNRs, respectively.

In the TEM images from drying in a magnetic field, while the large MagGNRs are well aligned parallel to **H**, the side-by-side distance (orthogonal to **H**) between the sides of neighboring MagGNRs is longer than the end-to-end distance (parallel to **H**) for MagGNRs arranged along the same line (Figure S3, Supporting Information). We attribute this to MagGNR–MagGNR (interparticle) magnetostatic (dipolar) interactions of coaligned magnetic domains, where side-by-side interactions are repulsive, and head-to-tail interactions are attractive. While the focus of this work is on well dispersed MagGNRs, such that these interparticle interactions are negligible, increasing the concentration during drying might increase these interparticle interactions and cause chaining.[81–83] In a control experiment, a TEM sample of MagGNRs prepared outside of the electromagnet was imaged and shown to have random orientation (Figure S4a,b, Supporting Information), confirming the role of the magnetic field for driving alignment of the MagGNRs.

2.4. Optical Extinction Spectroscopy

Extinction spectra of the MagGNRs closely resemble those of BSA-GNRs, with two notable differences (**Figure 3**a,b). The LSPR of the MagGNRs is redshifted because the coating of Fe_3O_4 NPs modifies the dielectric environment on the surface of the BSA-GNRs, which is a well-known effect.[49,65] The spectra of the MagGNRs also have a shoulder that is most prominent below ≈500 nm and is caused by the extinction of the Fe_3O_4 NPs in the blue. Most importantly, except for the redshift, there is no significant decrease in the intensity of the LSPR and minimal broadening, which we have directly confirmed in an additional mixing experiment (Figure S5, Supporting Information). The lack of significant extinction of the Fe_3O_4 NPs at the LSPR of the GNRs underscores the optical compatibility of these materials.

Extinction spectra in applied uniform magnetic fields were acquired by placing a compact spectrophotometer into the gap of an electromagnet (Figure S6, Supporting Information). For polarized measurements, incident light with propagation direction **k** was transmitted normally through a polarizer film and then through the cuvette, where **H** was fixed in the plane of the polarizer film. The polarization direction **P** could be oriented parallel or perpendicular to **H** (inset of Figure 3c). In an applied magnetic field of 10 kOe, the LSPR is enhanced
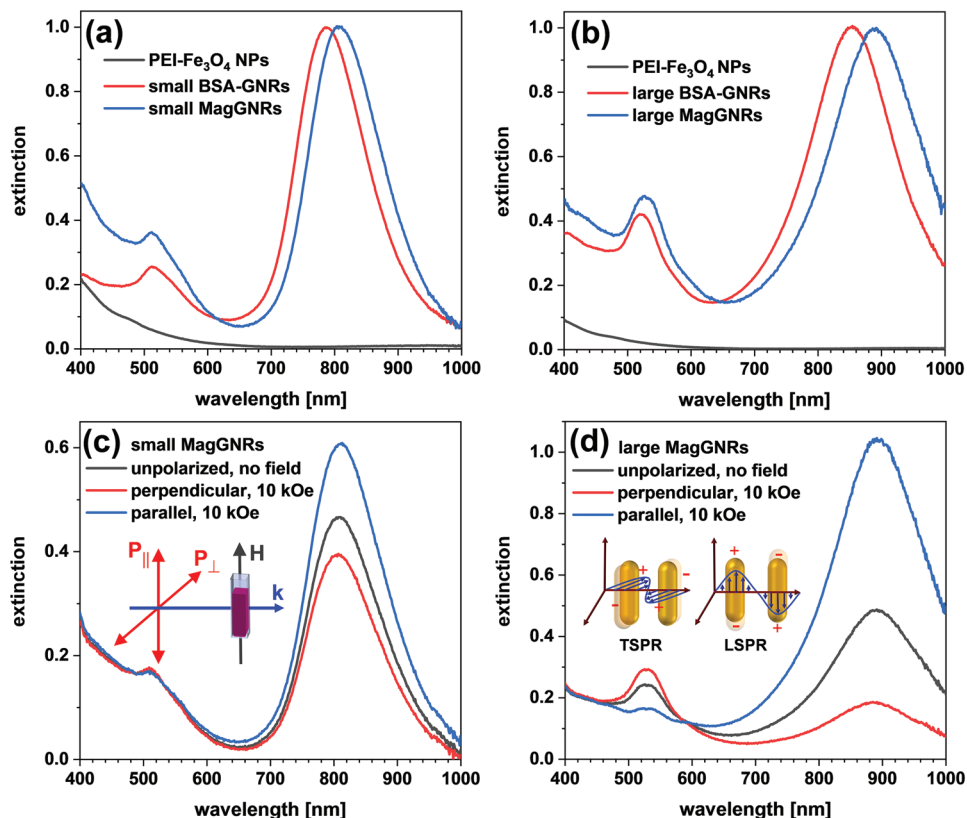
Figure 3. a,b) Optical extinction spectra of PEI-Fe_3O_4 NPs, BSA-GNRs, and MagGNRs for small (a) and large (b) GNR cores normalized at LSPR intensity of 1. The extinction of PEI-Fe_3O_4 NPs was normalized to the difference in the extinction of MagGNRs and BSA-GNRs at 400 nm. c,d) Unpolarized and polarized extinction spectra of MagGNRs in an electromagnet under zero field or uniform 10 kOe magnetic field for small MagGNRs (c) and large MagGNRs (d) without normalization. Both polarization directions **P** for light parallel or perpendicular to the magnetic field were measured.

(suppressed) and the TSPR is suppressed (enhanced) for light polarized parallel (perpendicular) to the direction of the applied magnetic field (Figure 3c,d). For large MagGNRs, there is an apparent isosbestic point at ≈590 nm. In the limiting case of perfect alignment of GNRs, light polarized parallel (perpendicular) to the long axis of the GNRs can be approximated as exciting solely the LSPR (TSPR). As such, the more prominent polarization dependence of the LSPR and TSPR observed for the large MagGNRs is consistent with more complete alignment than for the small MagGNRs. The same experiments have been conducted using smaller PEI-Fe_3O_4 NPs with a diameter of 6.6 nm (compared to 13.4 nm) on large GNR cores (Figure S7, Supporting Information). There is no obvious alignment of these MagGNRs by TEM, though evidence of minor alignment is observed in the polarized extinction spectra. The size of the Fe_3O_4 NPs is therefore an important parameter for obtaining alignment, where larger Fe_3O_4 NPs are needed for stronger dipolar coupling and substantially increasing $U_{barrier}$ above thermal energy. For all other experiments reported here, the larger Fe_3O_4 NPs with a diameter of 13.4 nm were used.

The extent of alignment, as characterized by the Maier–Saupe model of Equation (5) and trap depth parameter n, can be quantified from experimental polarized extinction spectra in applied magnetic fields. Specifically, measurements of the log_{10}-based extinction $A_∥$ and $A_⊥$ at the LSPR wavelength (810 and 891 nm for small and large MagGNRs, respectively) within a ±10 nm wavelength band were averaged to suppress noise for parallel and perpendicular configurations, respectively, under a field of 10 kOe. The values at each wavelength were treated as independent measurements and analyzed in two ways. First, the anisotropy ratio was computed, which can be related to the MagGNR angular distribution as follows (see the Supporting Information)

$$\frac{A_∥}{A_⊥} = \frac{\langle \cos^2 \theta \rangle}{\langle \sin^2 \theta \cos^2 \phi \rangle} = 2 \frac{\langle \cos^2 \theta \rangle}{\langle \sin^2 \theta \rangle} \tag{8}$$

Corresponding values of n were extracted by interpolating a curve of predicted anisotropy ratio versus n according to Equation (8) via numerical integration over the distribution of Equation (5). The resulting values were $n = 1.1$ and 4.5 for small and large MagGNRs, respectively. This highlights the dramatic increase in $U_{barrier}$, when the core GNR size is increased.

Second, a more common, 3D order parameter was computed

$$S_{3D,optical} = \frac{A_∥ - A_⊥}{A_∥ + 2A_⊥} = \frac{3 \langle \cos^2 \theta \rangle - 1}{2} \tag{9}$$

which is related to the underlying angular distribution (see the Supporting Information) and has been used extensively in other works.[26,29–31,84–86] S_{3D} has values between –0.5 and 1, where –0.5 indicates alignment perpendicular to the director, 0 indicates random alignment, and 1 indicates perfect alignment along the director. The measured $S_{3D,optical}$ for small and large MagGNRs in a 10 kOe magnetic field is 0.15 and 0.61, respectively. The latter is comparable to values for aligning dispersed GNRs with liquid crystals.[26,27,29]

Optical property measurements are also useful characterizing how the alignment of MagGNRs depends on the strength of the applied magnetic field. Polarized extinction spectra were acquired as a function of the applied magnetic field strength (**Figure** 4a,b), from which $S_{3D,optical}$ was calculated. There are only minor changes in the extinction for both polarization directions at fields above 500 Oe. The field dependence of $S_{3D,optical}$ was plotted (Figure 4c) to visualize this effect. At 4 kOe, $S_{3D,optical}$ is already saturated, and even at a much lower field of 250 Oe, $S_{3D,optical}$ is 91% of its maximum value at 10 kOe. In a control experiment, extinction spectra of BSA-GNRs without coatings of PEI-Fe_3O_4 NPs show no polarization dependence, confirming that they do not align in magnetic fields without the magnetic coatings (Figure S4c, Supporting Information). While others have demonstrated minor alignment ($S < 0.1$) of GNRs in extremely high magnetic fields (≈300 kOe), the extent of alignment at 10 kOe without magnetic overcoatings is negligibly small.[87]

H greater than 500 Oe can be easily obtained with permanent magnets, which give similar magnetic alignment to uniform magnetic fields without requiring an electromagnet. We observed that the intensities of the LSPR and TSPR can be modulated by moving the magnet to vary the angle of the magnetic field relative to a fixed polarization direction from 0° (parallel) to 90° (perpendicular) without substantially changing the field strength (Figure 4d). Light from the source propagates along **k** and through the polarizer film, sample, and detector, where the polarization direction **P** is orthogonal to **k** (inset of Figure 4d). A cylindrical magnet (1 in. diameter and 1 in. length) is placed with one pole facing the sample and with separation of 1 in. between the face of the magnet and the side of the cuvette. When **H** makes an angle of 90° (0°) with **P**, the TSPR (LSPR) is enhanced and LSPR (TSPR) is diminished.

2.5. Visualizing and Tracking Magnetic Fields

Evidence of the alignment of large MagGNRs in magnetic fields can be observed by eye using permanent magnets and polarizer films (**Figure 5**). For example, a large cube (1 in. edge) magnet oriented vertically generates vertical field lines on the top face but approximately horizontal field lines outside the edge of the top face, which is verified in a simulation of the magnetic field distribution (Figure S8, Supporting Information). Unpolarized photos of cuvettes placed in both the vertical and horizontal field regions do not show significant differences for the regions of different field orientation (Figure 5a), whereas the colors change to magenta and pale brown in polarized light (Figure 5b,c and Movie S1, Supporting Information). For polarization parallel (perpendicular) to the magnetic field, the longitudinal (transverse) mode is preferentially excited and thus appears pale brown (magenta). The pale brown color is caused by damping of the TSPR, but excitation of the LSPR is not apparent, because the LSPR peak is outside of the visible spectrum. A similar demonstration was performed using a circular Halbach array, which generates a more uniform magnetic field compared to single permanent magnet (Figure S9 and Movie S2, Supporting Information).

Using arrays of permanent magnets allows programming of the magnetic field throughout the volume of the solution, resulting in patterns of color based on alignment of the MagGNRs

ADVANCED
SCIENCE NEWS
www.advancedsciencenews.com

ADVANCED
MATERIALS
www.advmat.de
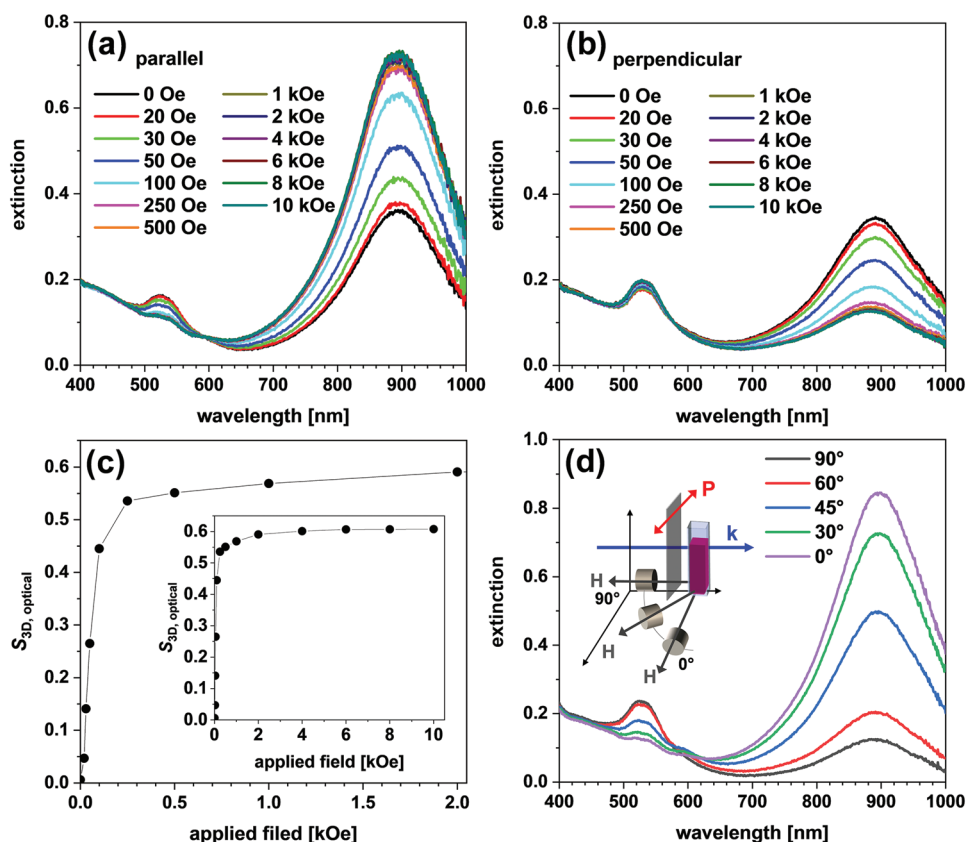
Figure 4. a,b) Polarized extinction spectra of large MagGNRs at different field strengths for light polarized parallel (a) and perpendicular (b) to the magnetic field using an electromagnet (same geometry as in Figure 3c). c) $S_{3D, optical}$ calculated from the polarized extinction at the LSPR as a function of applied field up to 2 kOe with inset showing up to 10 kOe. d) Polarized extinction spectra acquired with a cylindrical magnet placed at different angles with respect to the light polarization direction.

and the polarization state of the light. Patterns of both colors are observed under polarized light when the cuvette is placed between two parallel arrays of ¼ in. cube magnets (Figure 5d–f; Figure S10 and Movie S3, Supporting Information). The number and orientation of the magnets can further tune the color pattern as the magnetic field distribution changes (Figures S11–S13 and Movies S4–S6, Supporting Information). Magnetic separation is also noteworthy and can occur in a few minutes, when the magnets generate large magnetic field gradients. Soon after placing the cuvette between four 10 mm cube magnets, a central bright spot corresponding to a region depleted in MagGNRs grows as the MagGNRs are pulled toward the magnets (Figure 5g,h; Movie S7, Supporting Information). The separated MagGNRs collected on the wall of the cuvette show the region of high field gradient at the interface between permanent magnets (Figure 5i). The MagGNRs readily redisperse after removing the magnets with shaking or mild sonication.

The appearance in polarized and unpolarized light can be understood in greater detail based on the number of longitudinal and transverse modes excited for a given combination of orientations of **k**, **P** (which is always orthogonal to **k** in this work), and **H**. For randomly oriented GNRs in unpolarized light, there is one LSPR associated with the long axis and one TSPR associated with each of the two transverse axes. Aligning

MagGNRs in the plane of the polarizer film and orthogonal to **k** removes one of the TSPR modes and thus excites one LSPR and one TSPR for unpolarized light. Either mode can then be selectively excited with the polarizer, as in Figures 3c,d and 4a–c and Figures S9, S10a, S11a,b, S12a,b, and S13a,b (Supporting Information). In comparison, aligning the MagGNRs parallel to **k** (90° orientation in Figure 4d and Figures S10b, S11c, S12c, and S13c, Supporting Information) suppresses the LSPR and excites two TSPRs for unpolarized light or only one TSPR for polarized light, irrespective of the direction of **P**. Therefore, effects of magnetically aligning MagGNRs are also expected for unpolarized light but can be subtle and are enhanced with the polarizer. As already mentioned, the different colors observed in photographs and movies in this work arise predominantly from changes in the TSPR, because the LSPR is outside of the visible spectrum. It is important to note that we refer to unpolarized as ambient light that has not been purposefully polarized, but there can still be some unintended polarization from the light source and optical elements in the camera.

Dynamic magnetic alignment of the large MagGNRs can also be demonstrated by placing the cuvette on a magnetic stir plate, which generates a horizontal rotating magnetic field (Figure S14 and Movie S8, Supporting Information). The speed of oscillation of the colors tracks with the speed of the stir plate, even up to the maximum speed of 1000 rpm (16.7 Hz) (Figure S15

**ADVANCED
SCIENCE NEWS**

www.advancedsciencenews.com

**ADVANCED
MATERIALS**

www.advmat.de
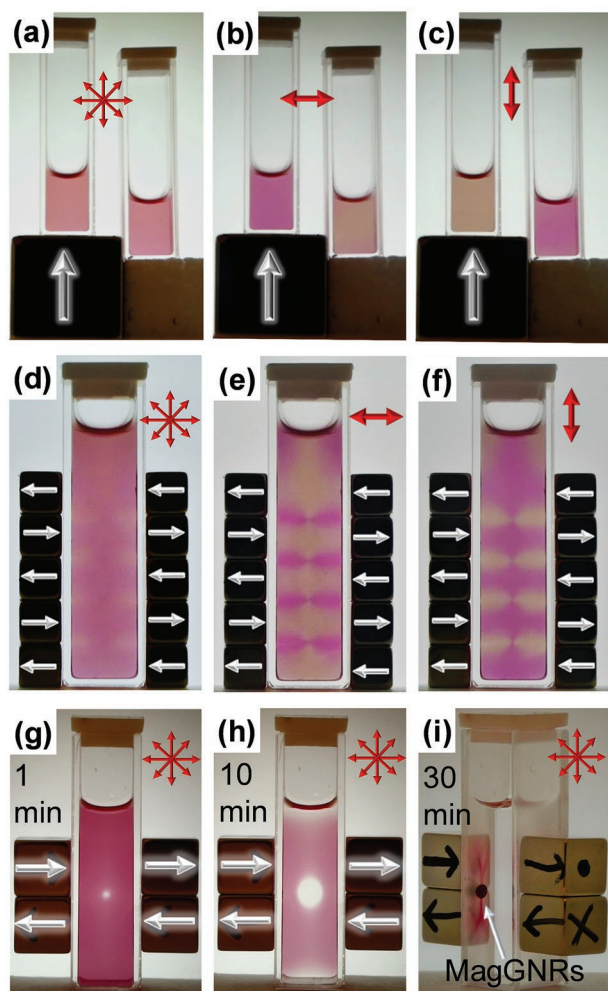
Figure 5. a–c) Photos of identical cuvettes with large MagGNRs placed on top of and next to the top face of a 1 in. cube magnet, unpolarized (a), with a horizontal polarizer (b), and with a vertical polarizer (c). d–f) Cuvette with large MagGNRs placed between arrays of ¼ in. cube magnets unpolarized (d), with a horizontal polarizer (e), and with a vertical polarizer (f). g–i) Nonuniform magnetic separation with four 10 mm cube magnets, where a central bright spot appears in unpolarized photos taken after 1 min (g), 10 min (h), and 30 min (i). The magnetization and polarizer directions are indicated by single-headed and double-headed arrows, respectively.

and Movie S9, Supporting Information). The rate of alignment and reorientation of MagGNRs could likely be increased by switching the magnetic field at higher frequency. For example, switching of GNRs with electric fields has been demonstrated at ≈kHz frequencies,[35,43] which implies that for low-viscosity solvents, hydrodynamics do not restrict faster switching than demonstrated here.

2.6. Small-Angle X-ray Scattering

SAXS measurements of dispersions of MagGNRs in magnetic fields of ≈2 kOe generated in the gap between permanent magnets provide another, direct structural measure of the alignment of MagGNRs dispersed in water. Large MagGNRs show

isotropic 2D scattering patterns without external magnetic fields, which become anisotropic when the MagGNRs align with the applied field direction (**Figure 6**a,b). The following directions and angles are depicted in Figure 1. The magnetic field creates an anisotropic scattering pattern that is more concentrated toward smaller $|q|$ values in the direction of **H**. The nanorod orientation is characterized by the polar angle θ between the long axis of the nanorod main axis **H**, which points along the x-axis. χ is the angle of the projection of the long axis of the nanorod in the viewing plane (xy-plane). Our analysis of the results closely follows recent work of Rosén et al.[88] Initially, the right half of 2D SAXS patterns, the half without the beam stop, was integrated into azimuthal distributions Ψ_χ by integrating over a range of q reflecting the characteristic sizes of the GNRs, i.e., in an interval $2\pi/L \leq |q| \leq 2\pi/d$,[88] where L and d are the length and diameter of the GNR core (excluding the Fe_3O_4 satellite NPs) obtained from TEM. After removing the background, Ψ_χ (Figure 6c,d) provides an estimate for the distribution of χ, the projected angle, which can be compared to the 2D distribution and analysis of TEM images (Figure S3, Supporting Information).

The distribution of the polar angle Ψ_θ can be calculated by fitting Ψ_χ with a linear combination of the first (3 and 5 for small and large GNRs, respectively, according to the criteria defined in ref. [88]) even Legendre polynomials. Assuming that Ψ_χ is axisymmetric about **H** (i.e., the x-axis), Ψ_θ can be reconstructed
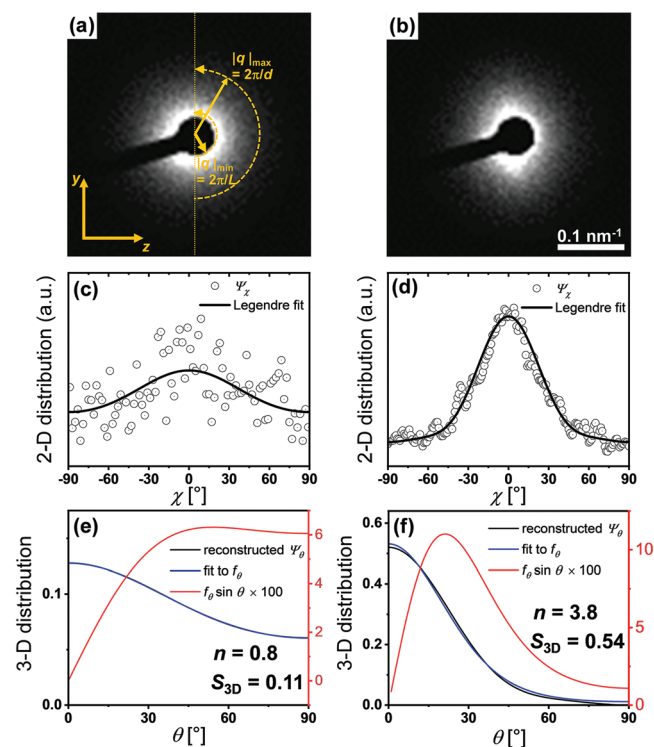
Figure 6. a,b) 2D SAXS patterns for large MagGNRs without external magnetic field (a) and with ≈2 kOe magnetic field (b). c,d) The azimuthal profiles under magnetic field of the projected angle χ and fit to a linear combination of Legendre polynomials for small (c) and large (d) MagGNRs. e,f) Reconstructed Ψ_θ and fit to f_θ, as well as the probability $f_\theta\sin\theta$, for small (e) and large (f) MagGNRs.

	H	n		S_{3D}		S_{2D}		θ_{RMS}	
		small	large	small	large	small	large	small	large
TEM	10 kOe	1.2	4.7	0.17	0.63	0.21	0.70	54°	33°
SAXS	2 kOe	0.8	3.8	0.11	0.54	0.14	0.61	57°	37°
Optical	10 kOe	1.1	4.5	0.15	0.61	0.19	0.68	55°	34°

$$n = U_{barrier} / k_B T$$

$$f_\theta \ n \ \sim e^{n\cos^2\theta}$$

$$S_{3D,SAXS} = \frac{3\langle\cos^2\theta\rangle - 1}{2}$$

$$S_{3D,Opt} = \frac{A_\parallel - A_\perp}{A_\parallel + 2A_\perp}$$

$$S_{2D,TEM} = 2\langle\cos^2\chi\rangle - 1$$

$$\left.\begin{array}{c} S_{2D,SAXS} \\ S_{2D,Opt} \end{array}\right\} = 2\langle\cos\theta\rangle - 1$$

$$\theta_{RMS} = \sqrt{\langle\theta^2\rangle}$$
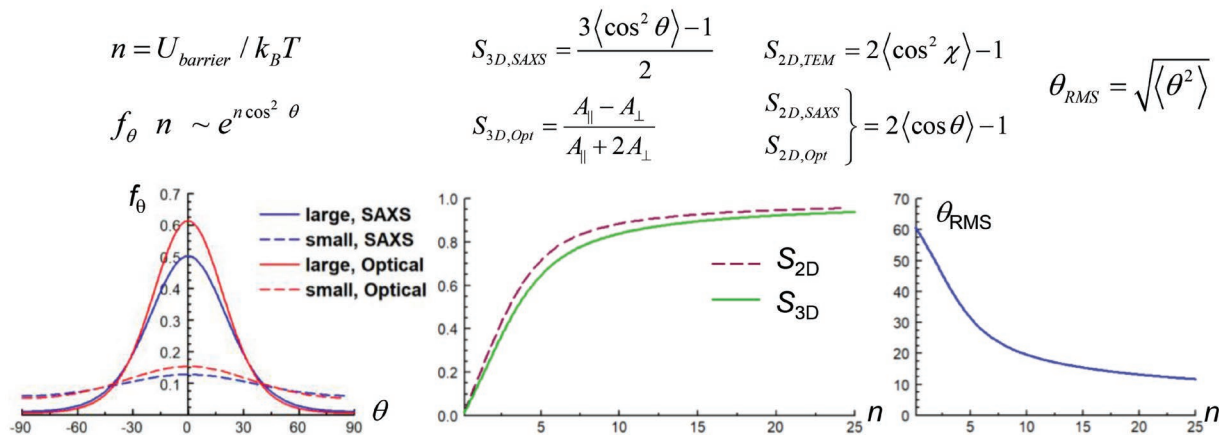
Figure 7. Top: Values of n, S_{2D}, S_{3D}, and θ_{RMS} extracted from TEM, SAXS, and optical extinction measurements for small and large MagGNRs under magnetic fields of strengths indicated. Middle: Associated expressions used for the calculations. Bottom: Plots of angular distribution functions (left) and dependence of S_{2D}, S_{3D}, and θ_{RMS} on n (middle and right).

from fitting Ψ_χ (Figure 6c,d) according to the previous work of Rosén et al.[88] To account for finite-size effects in the length of the nanorods and isotropic background, a Maier–Saupe distribution $f_\theta(n)$ (Equation (5)) was then fit to the reconstructed Ψ_θ distribution but with a free baseline,[89] because such behavior has been reported for other magnetically aligned nanorods.[78] The experimental data match well with $f_\theta(n)$ for the small and large MagGNRs with respective trap depth parameter n of 0.8 and 3.8 (Figure 6e,f). $f_\theta\sin\theta$ is also plotted and describes the probability of finding a MagGNR oriented at angle θ in the dispersion. From the fitted parameter n, which describes the width of the distribution, the order parameter $S_{3D,SAXS}$ can be obtained by combining Equations (5), (6), and (9)

$$S_{3D,SAXS} = \frac{\displaystyle\int_{-\pi/2}^{\pi/2}\left(\frac{3\cos^2\theta' - 1}{2}\right)e^{n\cos^2\theta'}|\sin\theta'|\,d\theta'}{\displaystyle\int_{-\pi/2}^{\pi/2}e^{n\cos^2\theta'}|\sin\theta'|\,d\theta'} \tag{10}$$

The order parameter $S_{3D,SAXS}$ for large MagGNRs is 0.54, which is much higher than 0.11 for small MagGNRs.

2.7. Summary of Analysis of Alignment of MagGNRs

As already discussed, each characterization method provides different primary data that allow for direct calculation of certain quantities—S_{2D} from TEM, S_{3D} from polarized extinction spectroscopy, and n from SAXS. Using the experimentally derived orientation distributions and the Maier–Saupe distribution as a model for magnetic alignment [Equation (5)], we extracted n for each method. From knowledge of n, we then computed S_{2D}, S_{3D}, and θ_{RMS} under this model [Equation (S24), Supporting Information, and Equation (7)], which are summarized in **Figure 7**. The estimates of $U_{barrier}$ based on n are largely consistent among all three characterization methods and for the larger MagGNRs are ≈ 4 times that of the small MagGNRs. The effect of this increase is apparent in the panel with the angular distributions, showing how small MagGNRs only exhibit partial alignment against the randomizing effects of Brownian motion, while large MagGNRs exhibit a narrowed distribution centered around the magnetic field direction at $\theta = 0$. As expected from the similar n, values of S_{2D}, S_{3D}, and θ_{RMS} are also largely consistent among all three methods. It is important to consider that $U_{barrier}$ depends on the magnetization of the Fe_3O_4 NPs. This might explain the slightly lower ordering observed by SAXS, where the weaker magnetic field nearly saturates the NPs, than for TEM and extinction spectroscopy measurements, in which stronger magnetic fields fully saturate the NPs.

These results also compare favorably with previous reports of the magnetic alignment of GNRs.[44–48] In those studies, the high polarization-independent background would reduce the optical anisotropy (Equation (8)) and $S_{3D,optical}$ (Equation (9)), even if the GNRs are physically well aligned. Deviations in the shape of the Au nanostructures from rods or high magnetic loading could contribute to increased background and broadening that might cause reduced ordering, as assessed optically instead of by TEM or SAXS measurements. Therefore, agreement in quantification from different characterization methods in this work suggests that there are minimal plasmonic shape impurities that could otherwise cause deviation.

It is also interesting to consider the 2D data collected as a function of the projected angle χ in the SAXS and TEM measurements. The distributions of χ obtained from TEM and

SAXS analysis agree quite well for large MagGNRs (Figure S3, Supporting Information). However, χ for small MagGNRs from TEM images does not match as well with the SAXS distribution. Since $U_{barrier}$ for small MagGNRs is smaller than for large MagGNRs, small MagGNRs might be more susceptible to drying effects when preparing substrates for TEM. Finally, the root-mean-squared polar angle θ_{RMS} displayed the same trend obtained by all three techniques.

2.8. Magnetic Property Measurements

Field- and temperature-dependent magnetometry measurements were performed on PEI-Fe_3O_4 NPs and large MagGNRs to investigate dipolar interactions within MagGNRs. Both samples were dispersed in poly(vinyl alcohol) (PVA) films to provide good dispersions. As expected, PEI-Fe_3O_4 NPs and MagGNRs are superparamagnetic at room temperature, based on the lack of magnetic hysteresis (**Figure 8**a). It is interesting to note that saturation of $S_{3D,optical}$ occurred at lower fields than magnetic saturation of the MagGNRs (Figure S16, Supporting Information). This different behavior is rooted in the field-dependence of $U_{barrier}$ for inter-acting superparamagnetic NPs, which is nontrivial to model and is beyond the scope of this work but is of interest for future studies.

Temperature-dependent measurements show the effects of dipolar interactions among Fe_3O_4 NPs on the surface of Mag-GNRs (Figure 8b,c). The sample is heated from 5 to 300 K in a measuring field of 10 Oe after cooling in a 10 Oe field (FC) or cooling in zero field (ZFC). The temperature at the maximum of the ZFC curve is defined as the superparamagnetic blocking temperature T_B, which is remarkably different for PEI-Fe_3O_4 NPs (109 K) and MagGNRs (177 K). The significant enhancement of T_B is consistent with an energetically stabilizing effect of dipolar coupling among Fe_3O_4 NPs on the surface of Mag-GNRs.[90,91] The flat shape of the FC curve for MagGNRs until reaching T_B further confirms strong coupling among the Fe_3O_4 NPs.[91] In contrast, in the FC curve of dispersed PEI-Fe_3O_4 NPs, the magnetization has significantly decreased before reaching T_B. In summary, magnetometry measurements support the proposed mechanism of magnetic alignment, where dipolar interactions among Fe_3O_4 NPs on the surface of the large MagGNRs result in $U_{barrier}$ large enough to give significant alignment.

3. Conclusions

For the magnetic alignment of nanostructures coated with magnetic satellite NPs, what is the smallest size that can still sufficiently overcome Brownian motion and align? While the size and aspect ratio of the core nanorod and the size and composition of the magnetic satellite NPs collectively determine this limit, we have experimentally demonstrated a new lower limit by aligning MagGNRs with low aspect ratios. These findings have implications for the magnetic alignment of all kinds of anisotropic nanostructures with magnetic satellite NPs. Large MagGNRs align well, while the small MagGNRs only give partial alignment. The underlying optical properties of the GNR cores are well preserved; GNRs that align in magnetic fields can be realized without degrading their optical properties. The multifunctionality of MagGNRs will be useful for several applications, including multimodal imaging and therapy, advanced (magneto-)optical materials based on the anisotropy and polarization effects of the plasmon, and magnetically modulated photothermal heating. Moreover, because the optical properties of the GNR cores are largely unchanged by the magnetic overcoating, MagGNRs will enable the further development of applications based on nonmagnetic GNRs that take advantage of the additional capability to manipulate MagGNRs with magnetic fields.

The performance of MagGNRs is promising for further investigation and applications. MagGNRs respond to low magnetic fields; anisotropy in the optical properties is already evident at 20 Oe, and nearly the maximum alignment is already obtained in fields of 500 Oe. MagGNRs can track dynamic fields of at least 17 Hz in water. This work introduces a comprehensive framework for analyzing the alignment of MagGNRs from their polarized optical properties and structural characterization, which yields the energy barrier that allows MagGNRs to overcome Brownian motion and align with the field. The model can further aid the design and analysis of the alignment of other small anisotropic nanostructures in magnetic fields or other fields or matrices that impart alignment.
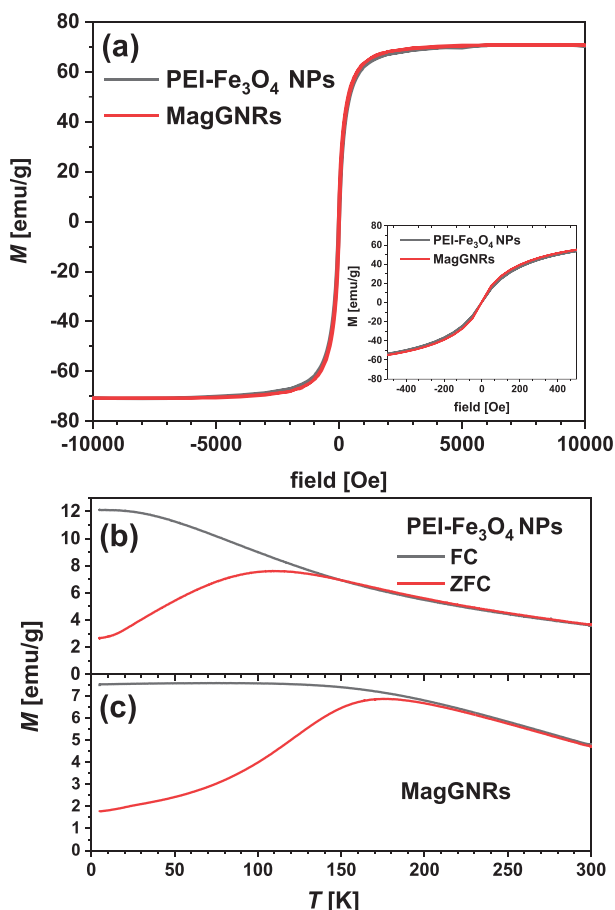
Figure 8. Magnetic characterization of PEI-Fe_3O_4 NPs and large Mag-GNRs in a PVA film. a) M versus H of PEI-Fe_3O_4 NPs and large MagGNRs at 300 K with inset showing the same plots magnified near the origin. b,c) Field cooled (FC) and zero field cooled (ZFC) measurements with a 10 Oe field of PEI-Fe_3O_4 NPs (b) and large MagGNRs (c).

4. Experimental Section

Chemicals: HAuCl$_4$·xH$_2$O (Alfa Aesar, 99.999%, where x was estimated as 3), CTAB (Amresco, high purity), KBr (Alfa Aesar, ACS, 99% min), AgNO$_3$ (Alfa Aesar, 99.9995%), deionized water (Ricca, ACS Reagent grade, ASTM Type I, ASTM Type II), ascorbic acid (AA, J.T. Baker, 99.5%), hydroquinone (Acros Organics, 99.5%), NaBH$_4$ (Sigma-Aldrich, 99%, 213462), NaOH (Sigma-Aldrich, 98%), BSA (Sigma-Aldrich, A7906, 98%), Na-citrate dihydrate (Mallinckrodt, 99% min), Fe(III) acetylacetonate (Strem, 99%), FeCl$_3$ (Alfa Aesar, anhydrous, 98%), Na oleate (TCI America, 97% min), oleic acid (Sigma-Aldrich, 90%), 1-octadecene (Sigma-Aldrich, 90%), benzyl ether (Acros Organics, 99%), oleylamine (Sigma Aldrich), hexanes (Macron, 95%), ethanol (Koptec, absolute, anhydrous), isopropanol (Macron, 99.5%), chloroform (OmniSolv, 99.9%), NaF (Alfa Aesar, 99.99%), 15-crown-5 ether (Ambeed, 98%), PEI (Alfa Aesar, branched, MW 10 000, 99%), and PVA (Alfa Aesar, 98%–99% hydrolyzed, high molecular weight) were used.

Permanent Magnets: 1 in. cube magnet (Diymag, N52), 10 mm cube magnets (Apex magnets, M10mmCU, N48), ¼ in. cube magnets (Bunting Magnetics, NEB38P252525, N38), and circular Halbach array (Supermagnetman, HB0060, field strength ≈1.8 kOe, N48) were used.

Synthesis and Purification of CTAB-Stabilized GNRs: Small CTAB-GNRs were synthesized following a previously published seed-mediated approach.[68] A typical 1 L synthesis yields ≈190 mg of CTAB-GNRs. The average dimensions of the GNR cores were 78 nm × 21 nm (aspect ratio of 3.7) with the LSPR peak extinction at 790 nm. Large CTAB-GNRs with average dimensions of 148 nm × 47 nm and peak LSPR extinction at 860 nm were also synthesized in two-step growth technique developed for this project. First, high-aspect-ratio CTAB-GNRs with dimensions of 117 nm × 21 nm were synthesized using another method,[69] in which 6 mL of seed solution was added to 250 mL of growth solution (0.5 × 10^{-3} M HAuCl$_4$, 100 × 10^{-3} M CTAB, 0.4 × 10^{-3} M AgNO$_3$, and 5 × 10^{-3} M hydroquinone) under gentle shaking and then aged for overnight. The seed solution was prepared by quickly injecting 0.6 mL of 10 × 10^{-3} M NaBH$_4$ solution into 9.4 mL of 0.5 × 10^{-3} M HAuCl$_4$ and 100 × 10^{-3} M CTAB that was rapidly stirring and already equilibrated in a water bath at 35 °C. Stirring was turned off 30 s after the injection, followed by aging for 25 min at 35 °C. For further growth into large CTAB-GNRs, 5 mL of the solution of as-prepared CTAB-GNRs was added to 20 mL of growth solution containing 91 × 10^{-3} M CTAB, 0.93 × 10^{-3} M HAuCl$_4$, 9.1 × 10^{-3} M KBr, and 0.992 × 10^{-3} M ascorbic acid. 1.1 mL of 15.76 × 10^{-3} M ascorbic acid was injected into this mixture over a period of 18 h with magnetic stirring at 35 °C. (As described, large excesses of small GNRs and of intermediate 117 nm × 21 nm CTAB-GNRs were synthesized, which allowed testing of multiple overgrowth reactions. In principle, these amounts could be scaled down.)

For both the small and large CTAB-GNRs, the concentration of CTAB before purification was ≈100 × 10^{-3} M. From each of the small and large CTAB-GNRs, a volume of 25 mL was purified in a single centrifuge tube. Both samples were purified in the same manner, three cycles of centrifugation (Thermo Scientific Sorvall Legend X1R with Fiberlite F15-6 × 100y rotor) at 10 000 rpm (10 956 g) for 20 min, which brought the final concentration of CTAB to ≈1 × 10^{-3} M. Between cycles of centrifugation, as much of the supernatant was carefully removed by pipette as possible, while avoiding perturbing the pellet of CTAB-GNRs. Water (after the first round of centrifugation) or 1 × 10^{-3} M CTAB (after the second and third rounds of centrifugation) was added to redisperse the pellet and bring the total volume to 25 mL after the first and second rounds and 10 mL after the third round of centrifugation.

Functionalization with BSA: BSA-GNRs were obtained from both small and large CTAB-GNRs by complete replacement of CTAB with BSA according to a previously reported method.[71] 20 mL of concentrated BSA solution (10 mg mL^{-1}) was prepared by mixing BSA with deionized water containing 0.02 wt% Na citrate. The mixture was sonicated for 10 min. 10 mL of deionized water was then quickly added (without mixing) to 10 mL of the purified CTAB-GNRs, which was then immediately transferred to the 20 mL BSA solution under sonication. Addition of deionized water destabilizes the CTAB-GNRs and facilitates replacement

of CTAB with BSA. The resulting 40 mL solution was sonicated for 30 min and then centrifuged at 9000 rpm (8875g) for 20 min. To ensure good BSA functionalization, the product was functionalized with BSA again, using a solution of BSA that was pH adjusted to ≈10, measured with a pH meter, as follows. 40 mg of BSA was dissolved in a mixture of 400 μL of 0.1 M NaOH and 39.6 mL of deionized water with 0.02 wt% Na citrate. The colorless supernatant was replaced with 40 mL of this 1 mg mL^{-1} BSA solution. The mixture was then sonicated for 5 min and kept at rest without stirring for 24 h before purification. The product was purified by four cycles of centrifugation, where the supernatant was replaced each time with 24.5 mL of basic water (pH ≈10.8, measured with a pH meter) that had been prepared by mixing 6 mL of 0.1 M NaOH in 194 mL deionized water. After purification, the BSA-GNRs were redispersed in 25 mL of the basic water.

Synthesis and Functionalization of Fe$_3$O$_4$ NPs with PEI: Oleylamine-stabilized magnetite (Fe$_3$O$_4$) NPs with an average diameter of 13.4 nm were synthesized in two steps. First, Fe oleate precursor was prepared and thermally decomposed, yielding oleic acid-stabilized NPs by following established methods.[72,92] In the second step, the oleic acid shell was replaced with oleylamine. Fe oleate was prepared by dissolving 3.244 g of anhydrous FeCl$_3$ with 18.27 g of Na oleate in a mixture of 30 mL of water, 40 mL of ethanol, and 70 mL of hexanes. The reaction was carried out by refluxing at 70 °C for 4 h with magnetic stirring. After completing the reaction, the top organic layer containing Fe oleate was separated from the aqueous layer and washed three times with water. The Fe oleate product was then dried in a fume hood for 2 d, during which the hexanes evaporated. For synthesizing Fe$_3$O$_4$ NPs, 2.5 g of Fe oleate and 1.26 g of oleic acid were dissolved in a mixture of 2.77 mL of benzyl ether and 5.55 mL of 1-octadecene in a three-necked round-bottomed flask and connected to a Schlenk line. The mixture was heated under vacuum to 60 °C for 30 min, followed by backfilling with nitrogen, then heating to 325 °C at a rate of 3.3 °C min^{-1}, and refluxing for 30 min to complete the reaction. After cooling to room temperature, 2 mL of the product was washed by adding a mixture of 2 mL of hexanes and 6 mL of ethanol, followed by centrifugation. After discarding the supernatant, the pellet was redispersed in 2 mL of hexanes, followed by addition of 6 mL of ethanol and centrifugation. After repeating this step once, the final pellet was dispersed in 20 mL hexanes.

A host–guest-driven technique was followed to replace the oleic acid with oleylamine,[73] as follows. 14 mL of isopropanol was added to the 20 mL of the Fe$_3$O$_4$ NPs in hexanes, followed by adding 2 mL of deionized water, into which 100 mg of NaF and 0.45 mL of 15-crown-5 ether had been dissolved. The mixture was sonicated for 5 min and then kept at rest for 2 h. As the oleic acid is stripped away, the Fe$_3$O$_4$ NPs agglomerate. The supernatant was discarded, and the product was successively washed with hexanes, isopropanol, water, and then ethanol. Each washing step was performed twice in ≈10 mL of each solvent before proceeding to the next solvent. The NPs were sonicated in each new solvent for 10 min, centrifuged at 5000–8000 rpm (2739–7012 g) for 20 min, redispersed in the same solvent again, sonicated for 10 min, centrifuged, and then redispersed in the next solvent. After the final washing step in ethanol, 9.98 mL of chloroform was added to the sedimented Fe$_3$O$_4$ NPs, followed by adding 20 μL of oleylamine and sonicating for 2 min. Oleylamine quickly regrafts onto the Fe$_3$O$_4$ NPs and causes them to disperse well. This solution was used as a stock solution and had a concentration of 1.48 mg mL^{-1} of Fe$_3$O$_4$ NPs, measured by inductively coupled optical emission spectroscopy (ICP-OES).

For functionalization with PEI, 1 mL of the stock solution of oleylamine-stabilized Fe$_3$O$_4$ NPs was diluted with 9 mL of chloroform. 100 mg of PEI was dissolved in 30 mL of chloroform and added to the diluted Fe$_3$O$_4$ NPs under vigorous stirring. The mixture was then sonicated for 30 min, followed by stirring at 40 °C for 2 h to complete PEI functionalization. The PEI-functionalized Fe$_3$O$_4$ (PEI-Fe$_3$O$_4$) NPs were there then transferred into water by adding 5 mL of water and shaking by hand for ≈1 min, until the brown color of the PEI-Fe$_3$O$_4$ NPs was visible in the top aqueous layer. The aqueous layer was then extracted and washed five times with deionized water to remove excess

PEI molecules. In each washing cycle, PEI-Fe_3O_4 NPs were purified using a centrifuge filter (Amicon Ultra, 100 kDa) at 3500 rpm (1342 g) for 30 min. The purified PEI-Fe_3O_4 NPs were dispersed in 2.5 mL of deionized water.

Assembly of MagGNRs: 0.5 mL of BSA-GNRs (concentration of ≈0.19 mg mL^{-1}, based on the extinction at 400 nm of 0.38 after 6× dilution) was added quickly to 0.5 mL of the purified PEI-Fe_3O_4 NPs (concentration of ≈0.6 mg mL^{-1}, based on effective 2.5× dilution of the above stock solution) under vigorous stirring (800 rpm) for 5 min. The mixture has pH of ≈10.6. The stirring rate was then decreased to 100 rpm for 2 h to complete the assembly of MagGNRs. Three cycles of centrifugation (Eppendorf 5415C Centrifuge, 5000 rpm [2152 g] for small MagGNRs and 2000 rpm [344g] for large MagGNRs) for 10 min were performed to separate MagGNRs from excess PEI-Fe_3O_4 NPs, where as much supernatant was removed as possible, and the product was redispersed in 1 mL of deionized water at the end of each cycle.

Transmission Electron Microscopy: TEM images were acquired on a FEI Talos F200X G2 at an operating voltage of 200 kV. Samples were prepared by drop casting onto a carbon-coated Cu TEM grid. For investigating magnetic alignment of MagGNRs, the TEM grid was placed between the poles (10 cm diameter) of a GMW 3472-70 electromagnet. A magnetic field of 10 kOe was applied while the solvent evaporated.

Optical Extinction Spectroscopy: Optical extinction spectra were acquired using an Ocean Optics Red Tide USB650 spectrometer with a glass cuvette having a 1 cm path length. The polarized extinction was measured by placing piece of a polarizer film (Thorlabs, LPNIRE2 × 2) in the beam path before the sample. For polarized extinction spectroscopy in applied magnetic fields, the spectrophotometer was placed between the poles of the electromagnet (Figure S6, Supporting Information), and polarizer films were inserted with their polarization axis either parallel (0°) or perpendicular (90°) to the magnetic field direction. To observe the effects of intermediate polarization angles between 0° and 90°, a single polarizer film was inserted next to the cuvette, and a permanent magnet was held at different angles with respect to the polarization direction (Figure 4d).

Small-Angle X-ray Scattering: SAXS measurements were performed on a Ganesha 300 XL+ (SAXSLAB) instrument with a focused X-ray beam from a Cu K$_\alpha$ source, giving $\lambda = 0.154$ nm. Scattered X-rays were recorded using a pixel detector (PILATUS 300 K) at a sample–detector distance of 1510 mm, enabling measurements down to $q_{min} \approx 0.035$ nm^{-1}. A glass capillary containing an aqueous dispersion of MagGNRs with extinction of ≈1 at the LSPR peak was oriented vertically along the y-direction and sandwiched between two permanent magnets, creating a quasi-homogeneous magnetic field oriented along the x-direction. A field of ≈2 kOe was generated by two cylindrical permanent NdFeB magnets (Supermagnete S-13-02-N, N45) with a diameter of 13 mm and a height of 2 mm, separated by a gap of 5 mm using a poly(tetrafluoroethylene) ring as a spacer. The orientation of MagGNRs can be defined with the polar angle θ between the long axis of the nanorod and the magnetic field direction (x-axis), and the projected angle χ in the xy-plane (Figure 1). The X-ray beam propagated in the z-direction, and the detector is in the xy-plane. Measurements were carried out in aqueous dispersions for 10 min. The solvent background was subtracted from the scattering patterns.

Magnetometry: PEI-Fe_3O_4 NPs and MagGNRs were dispersed in PVA films for magnetic characterization using a Quantum Design MPMS 3 superconducting quantum interference device vibrating sample magnetometer. Samples were prepared by dissolving 200 mg of PVA in 1 mL of water, followed by adding 0.01 mL of aqueous PEI-Fe_3O_4 NPs or MagGNRs, casting in a polytetrafluoroethylene mold, and allowing the water to evaporate overnight at 50 °C.

Statistical Analysis: TEM images are presented without contrast or brightness adjustment. Measurements of the dimensions and angular distributions of GNRs in TEM images were performed using ImageJ and were averaged over 200 GNRs. Optical extinction spectra are presented without smoothing. Statistical methods for analysis of SAXS measurements are described in Section 2.6. The SAXS data were processed using Matlab R2017b.

Supporting Information

Acknowledgements

Conflict of Interest

The authors declare no conflict of interest.

Data Availability Statement

The data that support the findings of this study are available from the corresponding author upon reasonable request.

Keywords

[1] L. M. Liz-Marzán, *Langmuir* **2006**, *22*, 32.

[2] X. Huang, I. H. El-Sayed, W. Qian, M. A. El-Sayed, *J. Am. Chem. Soc.* **2006**, *128*, 2115.

[3] L. Tong, Q. Wei, A. Wei, J.-X. Cheng, *Photochem. Photobiol.* **2009**, *85*, 21.

[4] R. K. Chhetri, R. L. Blackmon, W.-C. Wu, D. B. Hill, B. Button, P. Casbas-Hernandez, M. A. Troester, J. B. Tracy, A. L. Oldenburg, *Proc. Natl. Acad. Sci. USA* **2014**, *111*, E4289.

[5] M. R. K. Ali, Y. Wu, T. Han, X. Zang, H. Xiao, Y. Tang, R. Wu, F. M. Fernández, M. A. El-Sayed, *J. Am. Chem. Soc.* **2016**, *138*, 15434.

[6] I. Pastoriza-Santos, C. Kinnear, J. Pérez-Juste, P. Mulvaney, L. M. Liz-Marzán, *Nat. Rev. Mater.* **2018**, *3*, 375.

[7] J. Zeng, Y. Zhang, T. Zeng, R. Aleisa, Z. Qiu, Y. Chen, J. Huang, D. Wang, Z. Yan, Y. Yin, *Nano Today* **2020**, *32*, 100855.

[8] J. Lu, Y. Xue, K. Bernardino, N.-N. Zhang, W. R. Gomes, N. S. Ramesar, S. Liu, Z. Hu, T. Sun, A. F. d. Moura, N. A. Kotov, K. Liu, *Science* **2021**, *371*, 1368.

**ADVANCED
SCIENCE NEWS**

www.advancedsciencenews.com

**ADVANCED
MATERIALS**

www.advmat.de

[9] B. Nikoobakht, M. A. El-Sayed, *Chem. Mater.* **2003**, *15*, 1957.

[10] C. J. Murphy, T. K. Sau, A. M. Gole, C. J. Orendorff, J. Gao, L. Gou, S. E. Hunyadi, T. Li, *J. Phys. Chem. B* **2005**, *109*, 13857.

[11] W. Wei, F. Bai, H. Fan, *Angew. Chem., Int. Ed.* **2019**, *58*, 11956.

[12] J. Pérez-Juste, B. Rodríguez-González, P. Mulvaney, L. M. Liz-Marzán, *Adv. Funct. Mater.* **2005**, *15*, 1065.

[13] C. J. Murphy, C. J. Orendorff, *Adv. Mater.* **2005**, *17*, 2173.

[14] J. Li, S. Liu, Y. Liu, F. Zhou, Z.-Y. Li, *Appl. Phys. Lett.* **2010**, *96*, 263103.

[15] K. E. Roskov, K. A. Kozek, W.-C. Wu, R. K. Chhetri, A. L. Oldenburg, R. J. Spontak, J. B. Tracy, *Langmuir* **2011**, *27*, 13965.

[16] H. Zhang, Z. Hu, Z. Ma, M. Gecevičius, G. Dong, S. Zhou, J. Qiu, *ACS Appl. Mater. Interfaces* **2016**, *8*, 2048.

[17] P. Li, Y. Li, Z.-K. Zhou, S. Tang, X.-F. Yu, S. Xiao, Z. Wu, Q. Xiao, Y. Zhao, H. Wang, P. K. Chu, *Adv. Mater.* **2016**, *28*, 2511.

[18] W. Wei, Y. Wang, J. Ji, S. Zuo, W. Li, F. Bai, H. Fan, *Nano Lett.* **2018**, *18*, 4467.

[19] M. A. Correa-Duarte, N. Sobal, L. M. Liz-Marzán, M. Giersig, *Adv. Mater.* **2004**, *16*, 2179.

[20] D. Nepal, M. S. Onses, K. Park, M. Jespersen, C. J. Thode, P. F. Nealey, R. A. Vaia, *ACS Nano* **2012**, *6*, 5693.

[21] S. Nakamura, H. Mitomo, Y. Sekizawa, T. Higuchi, Y. Matsuo, H. Jinnai, K. Ijiro, *Langmuir* **2020**, *36*, 3590.

[22] H. Zhang, Y. Liu, M. F. S. Shahidan, C. Kinnear, F. Maasoumi, J. Cadusch, E. M. Akinoglu, T. D. James, A. Widmer-Cooper, A. Roberts, P. Mulvaney, *Adv. Funct. Mater.* **2021**, *31*, 2006753.

[23] F. Li, K. Wang, N. Deng, J. Xu, M. Yi, B. Xiong, J. Zhu, *ACS Appl. Mater. Interfaces* **2021**, *13*, 6566.

[24] M. Tebbe, M. Mayer, B. A. Glatz, C. Hanske, P. T. Probst, M. B. Müller, M. Karg, M. Chanana, T. A. F. König, C. Kuttner, A. Fery, *Faraday Discuss.* **2015**, *181*, 243.

[25] Y. J. Cha, D. S. Kim, D. K. Yoon, *Adv. Funct. Mater.* **2017**, *27*, 1703790.

[26] Q. Liu, Y. Cui, D. Gardner, X. Li, S. He, I. I. Smalyukh, *Nano Lett.* **2010**, *10*, 1347.

[27] M. R. Thomas, S. Klein, R. J. Greasty, S. Mann, A. W. Perriman, R. M. Richardson, *Adv. Mater.* **2012**, *24*, 4424.

[28] S. Umadevi, X. Feng, T. Hegmann, *Adv. Funct. Mater.* **2013**, *23*, 1393.

[29] Q. Liu, M. G. Campbell, J. S. Evans, I. I. Smalyukh, *Adv. Mater.* **2014**, *26*, 7178.

[30] Y. Zhang, Q. Liu, H. Mundoor, Y. Yuan, I. I. Smalyukh, *ACS Nano* **2015**, *9*, 3097.

[31] X. Liu, G. Qi, A. M. G. Park, A. Rodriguez-Gonzalez, A. Enotiadis, W. Pan, V. Kosma, G. D. Fuchs, B. J. Kirby, E. P. Giannelis, *Small* **2019**, *15*, 1901666.

[32] B. M. I. van der Zande, G. J. M. Koper, H. N. W. Lekkerkerker, *J. Phys. Chem. B* **1999**, *103*, 5754.

[33] W. Ahmed, E. S. Kooij, A. van Silfhout, B. Poelsema, *Nano Lett.* **2009**, *9*, 3786.

[34] J. Fontana, G. K. B. da Costa, J. M. Pereira, J. Naciri, B. R. Ratna, P. Palffy-Muhoray, I. C. S. Carvalho, *Appl. Phys. Lett.* **2016**, *108*, 081904.

[35] N. J. Greybush, K. Charipar, J. A. Geldmeier, S. J. Bauman, P. Johns, J. Naciri, N. Charipar, K. Park, R. A. Vaia, J. Fontana, *ACS Nano* **2019**, *13*, 3875.

[36] T. Fukagawa, R. Tajima, Y. Yamaguchi, H. Tanaka, K. Morikawa, S. Tanaka, Y. Hatakeyama, K. Hino, *J. Phys. Chem. C* **2021**, *125*, 11085.

[37] P. V. Ruijgrok, N. R. Verhart, P. Zijlstra, A. L. Tchebotareva, M. Orrit, *Phys. Rev. Lett.* **2011**, *107*, 037401.

[38] L. He, M. Wang, J. Ge, Y. Yin, *Acc. Chem. Res.* **2012**, *45*, 1431.

[39] M. Wang, Y. Yin, *J. Am. Chem. Soc.* **2016**, *138*, 6315.

[40] S. J. Hurst, E. K. Payne, L. Qin, C. A. Mirkin, *Angew. Chem., Int. Ed.* **2006**, *45*, 2672.

[41] B.-K. Oh, S. Park, J. E. Millstone, S. W. Lee, K.-B. Lee, C. A. Mirkin, *J. Am. Chem. Soc.* **2006**, *128*, 11825.

[42] M. K. Gupta, T. König, R. Near, D. Nepal, L. F. Drummy, S. Biswas, S. Naik, R. A. Vaia, M. A. El-Sayed, V. V. Tsukruk, *Small* **2013**, *9*, 2979.

[43] K. Kim, X. Xu, J. Guo, D. L. Fan, *Nat. Commun.* **2014**, *5*, 3632.

[44] I. Jung, H.-J. Jang, S. Han, J. A. I. Acapulco, S. Park, *Chem. Mater.* **2015**, *27*, 8433.

[45] I. Jung, H. Yoo, H.-J. Jang, S. Cho, K. Lee, S. Hong, S. Park, *Angew. Chem., Int. Ed.* **2018**, *57*, 1841.

[46] X. Wang, J. Feng, H. Yu, Y. Jin, A. Davidson, Z. Li, Y. Yin, *Research* **2018**, *2018*, 7527825.

[47] M. Wang, C. Gao, L. He, Q. Lu, J. Zhang, C. Tang, S. Zorba, Y. Yin, *J. Am. Chem. Soc.* **2013**, *135*, 15302.

[48] Z. Li, J. Jin, F. Yang, N. Song, Y. Yin, *Nat. Commun.* **2020**, *11*, 2883.

[49] C. Wang, J. Chen, T. Talavage, J. Irudayaraj, *Angew. Chem., Int. Ed.* **2009**, *48*, 2759.

[50] L. Huang, L. Ao, D. Hu, W. Wang, Z. Sheng, W. Su, *Chem. Mater.* **2016**, *28*, 5896.

[51] Z. Li, Y. Yin, *Adv. Mater.* **2019**, *31*, 1807061.

[52] Z. Li, Z. Ye, L. Han, Q. Fan, C. Wu, D. Ding, H. L. Xin, N. V. Myung, Y. Yin, *Adv. Mater.* **2021**, *33*, 2006367.

[53] Q. Wei, H.-M. Song, A. P. Leonov, J. A. Hale, D. Oh, Q. K. Ong, K. Ritchie, A. Wei, *J. Am. Chem. Soc.* **2009**, *131*, 9728.

[54] R. M. Erb, R. Libanori, N. Rothfuchs, A. R. Studart, *Science* **2012**, *335*, 199.

[55] X. Chen, Z. Ye, F. Yang, J. Feng, Z. Li, C. Huang, Q. Ke, Y. Yin, *Appl. Mater. Today* **2020**, *20*, 100749.

[56] M. Yan, J. Fresnais, J. F. Berret, *Soft Matter* **2010**, *6*, 1997.

[57] J. Townsend, R. Burtovyy, P. Aprelev, K. G. Kornev, I. Luzinov, *ACS Appl. Mater. Interfaces* **2017**, *9*, 22927.

[58] Z. Chen, J. Townsend, P. Aprelev, Y. Gu, R. Burtovyy, I. Luzinov, K. G. Kornev, F. Peng, *ACS Appl. Mater. Interfaces* **2018**, *10*, 11907.

[59] J. Yuan, H. Gao, F. Schacher, Y. Xu, R. Richter, W. Tremel, A. H. E. Müller, *ACS Nano* **2009**, *3*, 1441.

[60] B. Llerena Zambrano, C. Forró, E. Poloni, R. Hennig, P. Sivananthaguru, A. F. Renz, A. R. Studart, J. Vörös, *ACS Nano* **2022**, *16*, 837.

[61] M. A. Correa-Duarte, M. Grzelczak, V. Salgueiriño-Maceira, M. Giersig, L. M. Liz-Marzán, M. Farle, K. Sierazdki, R. Diaz, *J. Phys. Chem. B* **2005**, *109*, 19060.

[62] M. Zhang, D. J. Magagnosc, I. Liberal, Y. Yu, H. Yun, H. Yang, Y. Wu, J. Guo, W. Chen, Y. J. Shin, A. Stein, J. M. Kikkawa, N. Engheta, D. S. Gianola, C. B. Murray, C. R. Kagan, *Nat. Nanotechnol.* **2017**, *12*, 228.

[63] S. R. Mishra, M. D. Dickey, O. D. Velev, J. B. Tracy, *Nanoscale* **2016**, *8*, 1309.

[64] R. M. Erb, J. J. Martin, R. Soheilian, C. Pan, J. R. Barber, *Adv. Funct. Mater.* **2016**, *26*, 3859.

[65] B. S. Chapman, W.-C. Wu, Q. Li, N. Holten-Andersen, J. B. Tracy, *Chem. Mater.* **2017**, *29*, 10362.

[66] H. Chen, L. Shao, Q. Li, J. Wang, *Chem. Soc. Rev.* **2013**, *42*, 2679.

[67] J. Ge, Y. Hu, M. Biasini, W. P. Beyermann, Y. Yin, *Angew. Chem., Int. Ed.* **2007**, *46*, 4342.

[68] K. A. Kozek, K. M. Kozek, W.-C. Wu, S. R. Mishra, J. B. Tracy, *Chem. Mater.* **2013**, *25*, 4537.

[69] L. Vigderman, E. R. Zubarev, *Chem. Mater.* **2013**, *25*, 1450.

[70] B. N. Khlebtsov, V. A. Khanadeev, J. Ye, G. B. Sukhorukov, N. G. Khlebtsov, *Langmuir* **2014**, *30*, 1696.

[71] M. Tebbe, C. Kuttner, M. Männel, A. Fery, M. Chanana, *ACS Appl. Mater. Interfaces* **2015**, *7*, 5984.

[72] R. Chen, M. G. Christiansen, A. Sourakov, A. Mohr, Y. Matsumoto, S. Okada, A. Jasanoff, P. Anikeeva, *Nano Lett.* **2016**, *16*, 1345.

[73] B. S. Shaghasemi, E. S. Dehghani, E. M. Benetti, E. Reimhult, *Nanoscale* **2017**, *9*, 8925.

[74] E. C. Stoner, E. P. Wohlfarth, *IEEE Trans. Magn.* **1991**, *27*, 3475.

**ADVANCED
SCIENCE NEWS**

www.advancedsciencenews.com

**ADVANCED
MATERIALS**

www.advmat.de

[75] C. T. O'Konski, K. Yoshioka, W. H. Orttung, *J. Phys. Chem.* **1959**, *63*, 1558.

[76] W. Maier, A. Saupe, *Z. Naturforsch. A* **1959**, *14*, 882.

[77] W. Maier, A. Saupe, *Z. Naturforsch. A* **1960**, *15*, 287.

[78] B. J. Lemaire, P. Davidson, J. Ferré, J. P. Jamet, D. Petermann, P. Panine, I. Dozov, J. P. Jolivet, *Eur. Phys. J. E* **2004**, *13*, 291.

[79] Z. Hu, M. D. Fischbein, C. Querner, M. Drndić, *Nano Lett.* **2006**, *6*, 2585.

[80] I. Ahmad, H. P. Jansen, H. J. W. Zandvliet, E. S. Kooij, *Nanotechnology* **2015**, *27*, 025301.

[81] K. Butter, P. H. H. Bomans, P. M. Frederik, G. J. Vroege, A. P. Philipse, *Nat. Mater.* **2003**, *2*, 88.

[82] P. J. Krommenhoek, J. B. Tracy, *Part. Part. Syst. Charact.* **2013**, *30*, 759.

[83] J. B. Tracy, T. M. Crawford, *MRS Bull.* **2013**, *38*, 915.

[84] D. Yokoyama, A. Sakaguchi, M. Suzuki, C. Adachi, *Appl. Phys. Lett.* **2008**, *93*, 173302.

[85] D. Yokoyama, Y. Setoguchi, A. Sakaguchi, M. Suzuki, C. Adachi, *Adv. Funct. Mater.* **2010**, *20*, 386.

[86] E. C. Glor, R. C. Ferrier, C. Li, R. J. Composto, Z. Fakhraai, *Soft Matter* **2017**, *13*, 2207.

[87] P. G. van Rhee, P. Zijlstra, T. G. A. Verhagen, J. Aarts, M. I. Katsnelson, J. C. Maan, M. Orrit, P. C. M. Christianen, *Phys. Rev. Lett.* **2013**, *111*, 127202.

[88] T. Rosén, C. Brouzet, S. V. Roth, F. Lundell, L. D. Söderberg, *J. Phys. Chem. C* **2018**, *122*, 6889.

[89] S. Feng, X. Xiong, G. Zhang, N. Xia, Y. Chen, W. Wang, *Macromolecules* **2009**, *42*, 281.

[90] B. L. Frankamp, A. K. Boal, M. T. Tuominen, V. M. Rotello, *J. Am. Chem. Soc.* **2005**, *127*, 9731.

[91] F. Fabris, K.-H. Tu, C. A. Ross, W. C. Nunes, *J. Appl. Phys.* **2019**, *126*, 173905.

[92] J. Park, K. An, Y. Hwang, J.-G. Park, H.-J. Noh, J.-Y. Kim, J.-H. Park, N.-M. Hwang, T. Hyeon, *Nat. Mater.* **2004**, *3*, 891.

2203366 (14 of 14)